CHAPTER NINE

Mechanochemical Reactions of Metal-Organic Frameworks

Yu-Run Miao, Kenneth S. Suslick[1]
University of Illinois at Urbana-Champaign, Urbana, IL, United States
[1]Corresponding address: e-mail address: ksuslick@illinois.edu

Contents

Abstract

Metal-organic framework solids (MOFs) are synthetic porous materials that have drawn intense efforts in their synthesis and many of their chemical properties, most notably their use for the sorption of gases and vapors. The mechanical properties and mechanochemistry of MOFs, which we review in this chapter, have been only partially explored. MOFs can undergo both reversible, elastic deformations, and irreversible plastic deformations, some of which have associated mechanochemical reactions. During elastic deformation, MOFs undergo reversible structural or phase transitions. Plastic deformation of MOFs, on the other hand, can cause significant, permanent modification of the crystal structure, change in pore dimensions and configuration, and alteration of chemical bonding, all of which in turn affect their gas adsorption behavior. The large energies required to induce bond rearrangement during plastic deformation suggests an interesting potential of MOFs for shock wave mitigation applications.

Advances in Inorganic Chemistry, Volume 71
ISSN 0898-8838
https://doi.org/10.1016/bs.adioch.2017.11.001

1. INTRODUCTION

Metal-organic framework solids (MOFs), sometimes referred to as coordination polymers, have drawn intense interest in the chemical community in the past decade. They are constructed as "node-spacer" nanostructured materials (Fig. 1): metal centers (ions or clusters) are connected by organic linkers (commonly containing carboxylate or imidazolate groups) to form crystalline, extended, and often highly porous structures.[1–12] MOFs exhibit a variety of advantages over conventional porous materials: rationally designed synthesis of desired crystal structures and crystal engineering become feasible; great synthetic versatility and ease of incorporating different chemical functionalities; use of lightweight organic linkers that allow for ultrahigh surface area and porosity previously not accessible to conventional materials (i.e., zeolites and porous carbon). As a

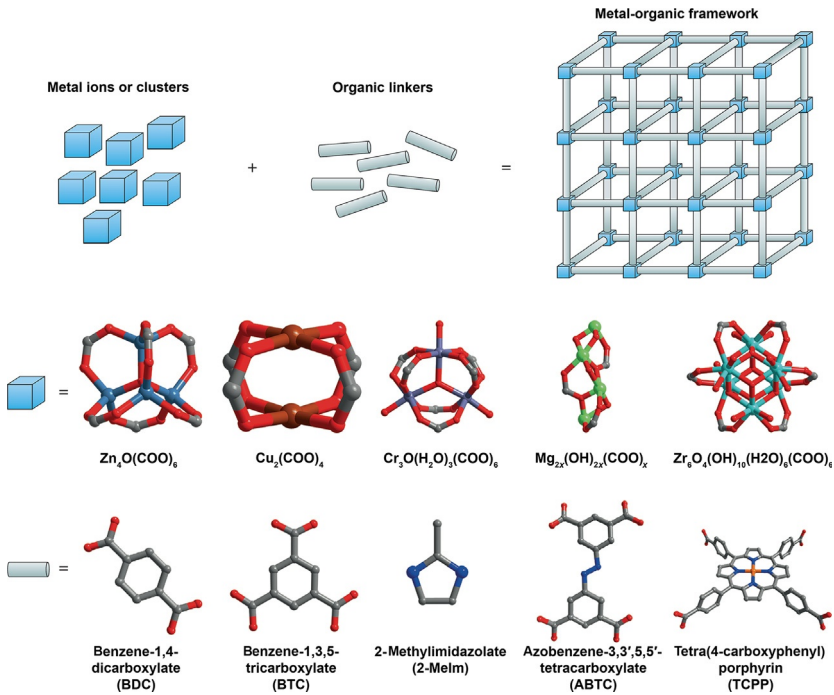

Fig. 1 The "node-spacer" structure of MOF and some of the representative metal centers and organic linkers. *Reprinted by permission from Macmillan Publishers Ltd.: Howarth, A. J.; Liu, Y.; Li, P.; Li, Z.; Wang, T. C.; Hupp, J. T.; Farha, O. K.* Nat. Rev. Mater. ***2016***, 1, *15018. Copyright 2016.*

consequence, MOFs show great promise for a rapidly expanding collection of applications, such as gas storage,[1,5,13,14] separations,[1,13,15–18] catalysis,[3,11,16,19,20] sensing,[21] and drug delivery.[11,22,23]

From preparation to application, any material will be subjected to mechanical stresses at one point or another in its processing, and MOFs are no exception. For example, the industrial applications of MOFs that involve cycles of pressurization/depressurization in gas sorption[24] demand a mechanical robustness that can prove problematic.[25,26] Even ZIF-8, a MOF well known for its exceptional chemical and thermal stability, loses some crystallinity just under manual packing.[27] There has been increasing recent interest in elucidating the mechanical behavior of MOFs. Understanding the origin of their mechanical vulnerability should provide further control over their structure–property relationships.[28,29] The geometry and topology of MOFs can be conveniently tuned by rational design, and the essentially unlimited combination of metal centers and ligands allows for systematic engineering of bonding modes and pore configuration, which in principal fundamentally governs their mechanical properties.

Recent years have also seen a rapid expansion of MOFs with "flexible" or "dynamic" features, in which the MOF can undergo substantial structural variation in response to external stimuli, such as solvent inclusion, thermal treatment, or light exposure.[6,30] Mechanical force, as a unique form of energy input, can also be applied to modify the MOF structure and consequently change gas adsorption and other properties. The large porosity of MOFs provides a high freedom for structural transitions at the molecular level, a deformation regime that is not possible for traditional dense materials. The inclusion of various guest species and their complex interaction with the framework can also fundamentally alter the behavior of MOFs. Furthermore, the structural deformation of MOFs may be utilized for the development of new protective or sacrificial materials that might divert destructive mechanical energy into the MOF framework to provide protection for personnel and equipment. All these features have begun to draw attentions to the emerging field of mechanochemistry in MOFs.

Mechanochemistry, the connection between the mechanical and the chemical worlds,[31–33] has its origins back in our earliest written records and beyond, from friction to fire.[34] Only in this past decade or so, however, has mechanochemistry gained a notable focus in the chemical community with the coming together of a huge diversity of related but quite different specialties, ranging from metallurgists to polymer scientists to synthetic organic and inorganic chemists to cellular biologists.[31–47]

In the following discussion, we present a general introduction to the complex mechanical and mechanochemical behavior of MOFs. The topic will be divided into two sections regarding the mechanochemistry of MOFs in the elastic and plastic deformation regimes, respectively, as they differ significantly in both structural responses and experimental approaches. Some interesting applications of MOFs related to the topic, such as mechanical energy storage, will also be covered.

2. CHEMICAL REACTIONS DURING ELASTIC DEFORMATION OF MOFs

2.1 Elastic Deformations of MOFs

For deformations that are less than the elastic limit (i.e., the limit of reversible mechanical behavior),[48,49] MOFs generally maintain their crystallinity and X-ray diffraction is a convenient method to scrutinize the structural changes. The most common experimental technique to obtain crystallographic information on MOFs under high pressure is diamond anvil cell (DAC) experiment.[50–52] In a DAC, the sample is sealed between two diamond anvils in a gasket chamber, which is filled with pressure-transmitting medium to apply uniform hydrostatic pressure. Usually a ruby chip is included in the chamber for the calibration of pressure using the wavelength shift of the ruby fluorescence. Spectroscopic measurements and single crystal or powder X-ray diffraction are then performed under hydrostatic compression up to several GPa. Mechanical properties, such as bulk modulus and compressibility can also be calculated from the measured lattice parameters as a function of applied pressure.

It is noteworthy that the hydrostatic compression of MOFs inherently will involve solvent effects, which is not generally the case with nonporous solids. The pressure-transmitting fluid used in DAC experiments can be penetrating or nonpenetrating, depending on whether the surface chemistry and size of the pores allows the molecules of the fluid to enter the pores of the MOF.[53–56] Such a fundamental difference among liquids leads to liquid-dependent responses from MOF crystals, even under the same applied pressure. For example, many MOFs undergo some framework *expansion* when initially external small molecule liquids are pushed into the available MOF porosity as solvates, often at relatively low pressures. In contrast, when compression is done using a nonpenetrating fluid, MOFs usually undergo monotonic volume *reduction* with increasing hydrostatic pressure. For penetrating fluids, the mechanical behavior of MOF under high-pressure is further

complicated by the potential that an intruding solvate molecule can cause structural changes even by themselves at ambient pressures (i.e., guest uptake induced flexibility or "breathing" behavior).

During hydrostatic compression of MOFs, some mechanical energy is stored or dissipated by means of the volume change of the pressurized medium. The energetics of MOF compression can be measured on a commercial liquid intrusion instrument: during the intrusion process, the nonwetting pressurized fluid with volume V is forced into the space occupied by MOF at pressure P and the mechanical energy stored (i.e., the work done by the external pressure) can be calculated as $E = \int P\mathrm{d}V$. The higher P and V, the more energy is absorbed. As before, the nature of the volume change is dependent on the fluid: the fluid can be forced into the pores if the fluid is penetrating, or it can induce structural contraction if it is nonpenetrating.

2.2 Pressure-Induced Reversible Chemical Reactions: Ligation and Deligation

In most reports on high-pressure experiment of MOFs, the structural transition phenomena are associated with changes in bond length and bond angle; the framework connectivity is usually retained without direct bond scission on the backbone of the framework. In some cases, however, the mechanochemical phase transition of MOFs can be caused by rearrangement of bonding that leads to fundamentally altered framework topology and connectivity.

Spencer et al.[57] reported the pressure-dependent structural evolution of a zinc imidazolate framework [Zn_2(imidazolate)$_4$] (ZnIm). At ambient pressure, this MOF crystallizes in an α phase that belongs to tetragonal space group $I4_1cd$. Each Zn center is surrounded by four N atoms from imidazolates in a distorted tetrahedral coordination environment and occupies the vertex site of a puckered square parallel to the *ab*-plane, with imidazolate located along the edge of the square. Under hydrostatic compression above 0.54 GPa, significant reduction in unit cell volume occurs that deviate from the calculation based on equation of state for α phase, indicating the formation of a new phase, β. Crystal structure reveals that the Zn-Im squares in β phase are rotated relative to each other and bridged at diagonal corners by imidazolate anions, resulting in contraction in the *ab*-plane and elongation in the *c* direction to accommodate the closer in-plane contact of Zn^{2+}.

A pressure-induced phase transition associated with a substantial bond rearrangement was observed in an Er MOF, $[tmenH_2][Er(HCOO)_4]_2$ ($tmenH_2^{2+}$ = *N*,*N*,*N*′,*N*′-tetramethylethylenediammonium, Fig. 2).[58] In this MOF, Er^{3+} ions are eight-coordinated by oxygen; each ErO_8 polyhedron is connected by $HCOO^-$ to neighboring Er atoms to form a layer parallel to the *bc*-plane, and adjacent layers are pillared by $HCOO^-$ bridges parallel to the *a*-axis. Under hydrostatic compression of 0.6 GPa, an abrupt phase transition with ~10% volume reduction occurs, primarily associated to the contraction along the *a*-axis. In the high-pressure phase, the chelating formate groups originally bound to individual Er^{3+} ions at ambient pressure are converted to bridging μ^2-ligands connecting two Er^{3+} ions in neighboring layers. Accordingly, additional linkages are formed along the *a*-axis, and the number of neighboring Er^{3+} connected to each Er^{3+} increased from 6 to

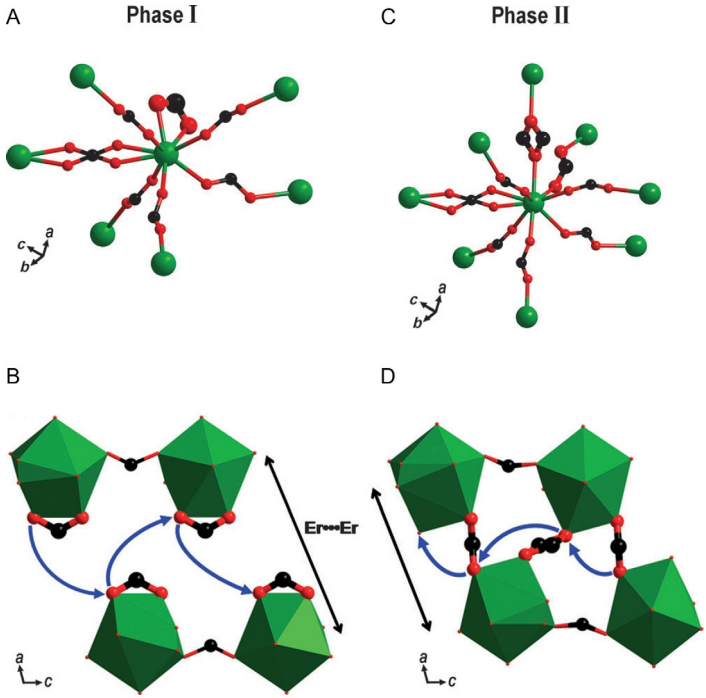

Fig. 2 (A and C) Coordination sphere for the Er^{3+} ions (*green* or *gray*) surrounded by formate ligands (*red* or *black*, hydrogen atoms not shown) and (B and D) the rearrangement of Er-formate coordination bond between phases I and II. *Adapted with permission from Spencer, E. C.; Kiran, M. S.; Li, W.; Ramamurty, U.; Ross, N. L.; Cheetham, A. K.* Angew. Chem. Int. Ed. ***2014***, 53, *5583–5586. Copyright 2014 John Wiley & Sons.*

8, while the symmetry and space group remains unchanged. This study presents a rare case of *reversible*, cooperative bond rearrangement in MOFs under pressure. In a separate indentation experiment, they also observed much higher resistance on the (001) face than on (100), which can be similarly attributed to the anisotropic linkages along these directions.

The scarcity of reversible pressure-induced bond rearrangement in MOF backbone may be a consequence of high strain and energy barriers associated with the structural transition. Coordination modification with solvents, however, can be achieved much more easily, especially for many MOFs that have unsaturated, labile metal centers lining the pores. Lanza et al.[55] reported pressure-induced nucleophilic addition of guest molecules in a flexible MOF, $Co_3(OH)_2btca_2$ (Co-btca, btca = benzotriazolide-5-carboxylato). The as-prepared crystals have two independent unsaturated Co sites (Fig. 3) and contain two DMF molecules per $Co_3(OH)_2btca_2$ formula unit that are trapped in the channels through hydrogen-bonding interactions with the framework μ_3-OH groups. During compression in a nonpenetrating fluid, the crystal is readily transformed to a P-1 phase at 0.4 GPa, with a greatly reduced Co–O_{DMF} distance, 2.383 (18) Å compared to 3.440 (9) Å at room pressure, and a dramatic change in Co stereochemistry, suggesting an extracoordination of DMF at one of the unsaturated Co sites. Further compression up to 3.6 GPa significantly reduces the volume by 17%, primarily along the direction that corresponds to contraction of the channel opening, and DMF molecules in the pores are forced to reorient parallel to the pore walls. When methanol/ethanol mixture is used as a penetrating medium, the DMF solvate molecules are readily exchanged with methanol, and the crystal expands at low pressures due to "superfilling." At 0.3 and 2.2 GPa, two methanol molecules are sequentially added to the two coordination sites, resulting in a fully packed, saturated framework; upon release of the external pressure, the methanol ligation is lost and the structure reverts. The two newly formed Co–O_{MeOH} bonds are both 2.354 (17) Å, indicating equivalency of the two coordination sites.

In another example of reversible pressure-induced coordination chemistry, McKellar et al.[59] conducted high-pressure diffraction experiment on STAM-1, a MOF based on dimeric paddle-wheel Cu centers connected by monomethyl-esterified BTC (benzene-1,3,5-tricarboxylate) linkers. Similar to Cu-BTC, each of the Cu centers in STAM-1 is surrounded by four equatorial oxygen from BTC carboxylates and an axially coordinated oxygen from water molecules that point into the pores. The Cu-bound water molecules can exchange with various organic solvents both at ambient

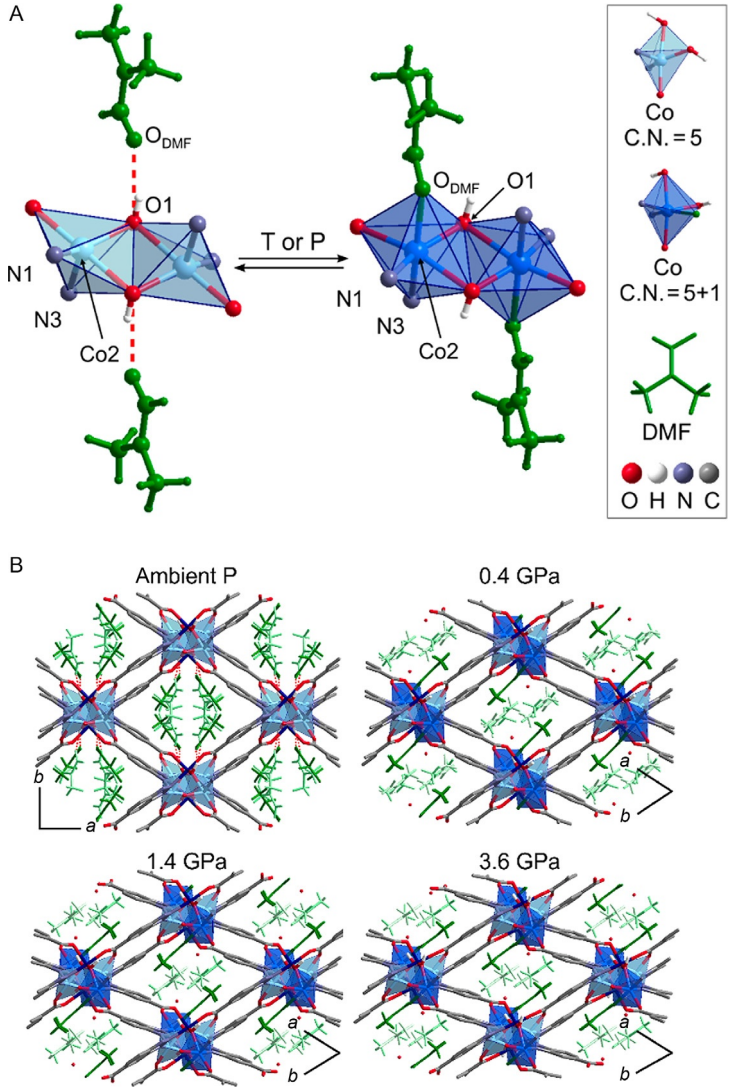

Fig. 3 Structural changes of Co-btca under hydrostatic compression in a non-penetrating fluid. (A) Coordination mode change of Co centers. Coordination polyhedral in *light blue* or *gray* (five-coordinated) or *dark blue* or *gray* (six-coordinated). (B) Packing of Co-btca as a function of applied pressure. Coordinated and disordered uncoordinated DMF molecules are colored in *dark and light green* or *gray*, respectively. *Reprinted with permission from Lanza, A.; Germann, L. S.; Fisch, M.; Casati, N.; Macchi, P.* J. Am. Chem. Soc. ***2015***, 137, *13072–13078.*

and above-ambient pressures, which dramatically changes the size and surface hydrophobicity of the pores. In methanol, the structure is stable up to 5.7 GPa because methanol can readily exchange with the coordinated water molecule and essentially fill all the void space in the framework, thus providing additional resistance to mechanical stress. In contrast, in the compression experiment with isopropanol, which is too large to fit into the smaller channels and can therefore only fill half of the total void space, the crystal shattered at only 2.4 GPa. The crystal becomes polycrystalline upon exposure to ethanol even at ambient pressure, which is attributed to strain-induced collapse of the framework caused by steric hindrance and energetically unfavorable environment in the smaller, more hydrophilic pores.

3. MECHANOCHEMISTRY DURING PLASTIC DEFORMATION IN MOFs

Within the elastic regime, the temporary deformation of MOF structure is recovered after the release of mechanical stress. However, more severe mechanical treatment (which includes ball milling, bulk compression, strong hydrostatic compression, and shock impact) can result in stresses beyond the elastic limits of MOFs and cause *irreversible*, plastic deformation. Associated with the plastic deformation is mechanochemical consequences that result from partial or complete loss of crystallinity and porosity with the accompanying distortion and changes to local bonding structure.

Such plastic deformation can have useful applications, for example, as a means to modify the porosity of MOFs and control diffusion kinetics of guest molecules. Moreover, the mechanical environment may also trigger unconventional chemical reactivity and point to convenient routes for the solvent free synthesis of MOF structures.[60–62] Finally, very large mechanical energy absorption can occur during plastic deformation which suggests the potential of MOFs in shock dissipation applications.

3.1 Amorphization and Densification of MOFs

During plastic deformation, the state and structure of a MOF are affected by a variety of factors, including the nature of the mechanical effect (bulk compression, ball milling, DAC, etc.), intensity of the mechanical action, and its duration. The structural evolution of MOFs during mechanical action is often associated with a decrease in crystallinity and porosity. These effects are most commonly characterized ex situ, i.e., at the end of mechanical action or after the release of applied pressure. The most common techniques

for ex situ characterization are X-ray diffraction (usually of powder) and gas adsorption porosimetry. Recent advances in total scattering analysis also provide, in principle, a more detailed analysis of the amorphized structure.[63,64] There have also been recent advances of in situ characterization of MOFs during mechanical action (specifically ball milling), and the experimental apparatus for in situ monitoring of the mechanochemical processes has provided valuable information on the reaction progress and underlying mechanism.[61,65–68]

3.1.1 Ex Situ Characterization

Chapman et al.[27] reported pressure-induced amorphization of ZIF-8 in a hydraulic pellet press at applied pressures up to 1.2 GPa. From the N_2 adsorption experiment of the amorphized products, significant modification in the isotherms was observed: while the total uptake is systematically reduced after increasing compression, there is actually increased sorption after compression at low pressures, accompanied by the gradual disappearance of multistep features in gas uptake profile of untreated ZIF-8 samples. This observation is interpreted in terms of homogenization of pore/window dimensions in ZIF-8. Computation results show that the mechanical instability of ZIF-8 originates from its low shear resistance against stress.[69,70] Cao et al.[71] found that ZIF-8 can also be amorphized rapidly under ball milling into a solid product with increased density and reduced porosity and that the conversion depends on milling time. In a total scattering analysis, the amorphous product matches well with a continuous random network structure modeled from the topology of silica glass, in which the short-range order of the original ZIF-8 framework is retained.

The time needed to amorphize porous materials under prolonged mechanical treatment (e.g., ball milling) can be used as an indication of their relative structural stability. Baxter et al.[72] investigated the amorphization kinetics of several ZIF materials under ball milling and compared to that of aluminosilicate zeolites to identify the key structural parameters in determining the structural stability. The classical inorganic zeolites, including Na–X, Na–Y, and ZSM-5, amorphize four times slower than ZIFs. Among the Zn-containing ZIFs, the rates of amorphization increase following the trend of solvent accessible free volume in the structure. Furthermore, the cadmium derivative of ZIF-8 amorphizes at a faster rate than Zn ZIF-8, which can be ascribed to the relatively weak M–N bond.

Bennett et al. reported mechanical amorphization of several crystalline polymorphs of ZIF-4, a zinc imidazolate ZIF, via ball milling for

30 min[60]; ball milling greatly reduced the time needed for amorphization compared to only heating. Total scattering analysis indicates the amorphized products from different precursors are indistinguishable from each other. In contrast, high-pressure compression using DAC experiments on ZIF-4[73] demonstrate a rare phenomenon that the crystal undergoes *reversible* amorphization irrespective of pore occupancy, and the transition takes place at different applied pressures depending on the pressure-transmitting fluid. When the pores are filled with solvate molecules, an intermediate phase of ZIF-4-I emerges before the transition to amorphous state.

Hu and Zhang[74] conducted bulk compression of MOF-5 and found the sample was irreversibly amorphized at ambient temperature by employing a low compressing pressure of 3.5 MPa with complete loss of porosity. The vibrational modes of the Raman spectra of the amorphized sample are similar to that of a pristine sample, although changes in the relative intensity of the bands indicate the amorphization was caused by destruction of some carboxylate groups. Banlusan et al.[75] performed large-scale molecular dynamics (MD) simulation on MOF-5 to resolve the structural mechanism for the plastic deformation of MOF-5 under uniaxial compression. They found that the deformation can be primarily attributed to the structural collapse of the 001 plane that involves slip along the ⟨100⟩ direction, facilitated by the flexible bonds between Zn–O clusters and BDC ligands.

3.1.2 In Situ Characterization

Monitoring the evolution of structure in situ during mechanochemical reactions of solids can provide very useful information for understanding reaction kinetics and underlying mechanisms. Friščić and coworkers developed a milling system that enables in situ and real-time analysis of mechanochemical reactions by synchrotron X-ray diffraction.[61,66] In this regard, it is possible to track the progress of reaction and identify the often metastable intermediate species during the mechanochemical synthesis and conversion of MOFs.

The use of mechanochemistry for the synthesis of MOFs has also been reported.[62] Several ZIF phases can be obtained from a liquid-assisted grinding synthesis using ZnO and imidazole type ligands, and the addition of ammonium salts greatly accelerates the reaction rate. With the in situ monitoring system, the reaction kinetics of the MOF synthesis have been studied in some detail.[67] The growth kinetics of crystalline ZIF-8 exhibits a sigmoidal curve, indicating a mechanism that involves nucleation and growth of crystallites from amorphous matrix. The reaction between ZnO and 2-ethylimidazole proceeded through several intermediate phases with

zeolitic topologies[76] of RHO, ANA, and β-quartz, and reaction between ZnO and imidazole afforded several distinct products depending on the choice of grinding liquid. The complicated evolution of multiple phases that appeared during the mechanochemical synthesis of ZIF-8 was further investigated by Katsenis et al.[65] (Fig. 4). In the presence of small amounts of water or water/acetic acid mixture, they observed immediate formation of ZIF-8 upon ball milling, followed by gradual amorphization. Extending the ball milling over 50 min transformed ZIF-8 into a new phase that they termed katsenite, although the exact time of appearance of the new phase was difficult to reproduce, possibly stemming from the stochastic processes of nucleation from an amorphous matrix. The metastable katsenite phase is readily converted to a nonporous cubic diamond phase with mild heating, exposure to organic solvents, or further ball milling. Interestingly, the dried amorphous phase can be recrystallized to ZIF-8 upon liquid-assisted milling in the presence of DMF.

Contrary to the common observation that prolonged ball milling leads to increased framework density, the mechanochemical synthesis of Zn-MOF-74[68] first produced a dense phase before the formation of the porous MOF-74 framework. It was proposed that the highly reactive carboxylic groups on the ligand first coordinated with Zn, which corresponds to the dense phase, and then gradually coordinated to the less reactive phenol groups forming crystalline MOF-74. These studies illustrate that the application of dynamic mechanical stress, such as ball milling, may provide unique mechanochemical environments not routinely accessible by conventional chemistry.

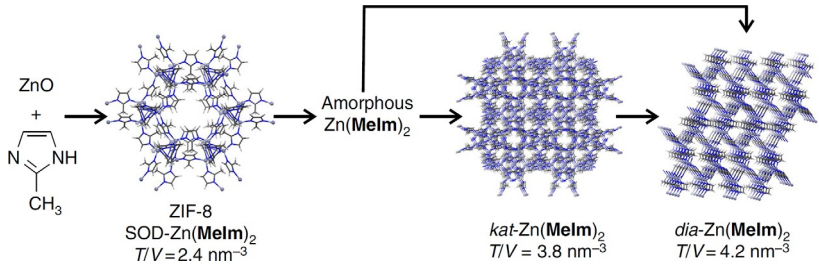

Fig. 4 The evolution of structures presents during the balling milling of ZnO and 2-methylimidazole. The transformation of ZIFs follows the order of increasing *T/V* value with increased thermodynamic stability. *Reprinted by permission from Macmillan Publishers Ltd.: Katsenis, A. D.; Puškarić, A.; Štrukil, V.; Mottillo, C.; Julien, P. A.; Užarević, K.; Pham, M.-H.; Do, T.-O.; Kimber, S. A. J.; Lazić, P.; Magdysyuk, O.; Dinnebier, R. E.; Halasz, I.; Friščić, T.* Nat. Commun. ***2015***, 6, *6662. Copyright 2015.*

3.1.3 Effect of Densification on Sorption Properties

MOFs are typically synthesized in the form of loose powders, which require further processing, shaping, or recrystallization to be integrated into a functional module for industrial applications or further characterization (e.g., single crystal X-ray diffraction). In addition, for applications where the *volumetric* adsorption capacity, rather than the *gravimetric* capacity, is critical (e.g., vehicular storage of hydrogen or methane), loose powders are suboptimal.[25] Therefore, there is a practical need to study the effect of compression on densification of MOFs and their adsorption performance.

In order to improve the volumetric density and thermal conductivity of MOF-5 by mechanical compaction, Purewal et al. shaped MOF-5 powder into tablets having controllable densities up to 1.6 g/cm^3, as compared to the very low 0.13 g/cm^3 apparent density of the pristine powder.[77] From their observation, a significant portion of the pelletized MOF-5 remains crystalline even at an applied pressure of 80 MPa and a resulting pellet density of 0.75 g/cm^3. Although the gravimetric BET surface area and pore volume, along with H_2 uptake, decreases gradually as the powder becomes more compacted, the *volumetric* hydrogen adsorption capacity reaches a maximum of 26.0 g/L at 0.51 g/cm^3, which is a 350% increase relative to the initial powder and about 70% of the theoretical value calculated from H_2 adsorption isotherms and crystallographic density of the single crystal.

Another long-lasting concern for the industrial application of many MOFs (and MOF-5 specifically) is their low chemical stability toward moisture[78]; for MOF-5, this rapidly reduces the H_2 adsorption capacity upon exposure to humidity. To tackle this problem, Ming et al.[79] measured the adsorption properties of MOF-5 as a function of humidity level, exposure time, and sample compaction (i.e., powder vs pellet). While the gravimetric H_2 storage capacity of pelletized MOF-5 suffers from the compaction, its kinetic stability to hydrolytic degradation is significantly improved. For example, it only takes 2 h to observe a significant decrease in H_2 uptake in powder MOF-5 at 45% relative humidity, whereas after pelletization, ~24 h is needed to suffer a comparable loss in porosity. The improved resistance of the pelletized MOF-5 to moisture is attributed to the reduced permeation from densification that affects both concentration and diffusivity of water vapor.

Peterson et al.[80] pelletized two other archetypical MOFs, UiO-66 and Cu-BTC, at pressures of 1000 and 10,000 psi, and found neither material showed signs of significant structural degradation. In another study on pelletized UiO-66-NH_2,[81] the structure remains intact up to 25,000 psi with a

slight decrease in surface area. The granules made from powder compressed at 5000 psi were tested in breakthrough experiments against ammonia and cyanogen chloride to simulate the application for air filters and respirator cartridges. In spite of the high equilibrium adsorption capacity measured under isostatic conditions, the dynamic breakthrough time measured for both gases was significantly shorter than the values measured for porous carbon, possibly due to the limited mass-transfer kinetics through the porosity. In contrast, a recent simulation study predicts that tensile deformation of ZIF-8 may induce a "gate-opening" effect that could improve the diffusion rate of gas sorbents through the pores.[82]

3.1.4 Amorphous MOFs for Controlled Release and Sequestration

Amorphization of MOFs and the concomitant reduction in pore volume and aperture size may detrimentally affect their adsorption performance, but it may also become a simple method to control the kinetics of guest diffusion in MOFs postsynthetically without the complications of wet chemistry, which could have advantages for some applications, such as the permanent storage of harmful chemicals. For example, radioactive iodine (^{131}I) in the form of I_2 is a gaseous waste product from nuclear fission and can be adsorbed by ZIF-8 at a capacity of 5.4 I_2 per ZIF-8 cage.[83] Chapman et al.[84] studied the sequestration of I_2 from pressure-amorphized ZIF-8 that had been preloaded with I_2. Pair distribution function analysis shows that the local interaction between I_2 and the framework is not altered upon amorphization, and it is concluded that the reduction of aperture size in ZIF-8 created a kinetic barrier for the iodine release and hence improved I_2 retention. Amorphization of ZIF-8 and another isostructural MOF, ZIF-mnIm ($Zn(mnIm)_2$ where mnIm = 4-methyl-5-nitroimidazolate), during ball milling[85] also significantly enhances their iodine retention abilities, particularly in the case of ZIF-mnIm. For comparison, pressure-amorphized ZIF-8 will release iodine and lose weight at 200°C,[83] whereas this is not true for ball milled amorphized samples. This distinction is associated with the complete loss of porosity in ZIF-8 under ball milling, in contrast to pressurized ZIF-8 where only part of the pore access is collapsed. It was also observed that ZIF-69, with the largest aperture among the ZIFs tested in the study, has the highest I_2 adsorption capacity but the poorest retention ability.

The kinetic slowing of guest release in amorphized MOFs can also be utilized for controlled drug delivery. Orellana-Tavra et al.[86] encapsulated a hydrophilic model molecule calcein (a derivative of fluorescein dye)

into UiO-66, followed by ball milling amorphization of the framework. In a mock drug delivery test, calcein in amorphous UiO-66 was slowly released over a period of 30 days, as opposed to the complete release in only 2 days from crystalline UiO-66. The study was extended to explore the drug delivery performance of an isostructural series of UiO MOFs with varied linker length and pore size. Using an anticancer drug, α-cyano-4-hydroxycinnamic acid (α-CHC),[87] however, showed no difference between crystalline and amorphous MOF, indicating the necessity to balance the pore size of MOFs and size of guest molecules to achieve successful and efficient control over the drug release process.

3.2 Plastic Deformation and Mechanical Energy Absorption

Most of the previous reports on mechanical energy absorption of MOFs examine only the regime of *reversible* volume changes (i.e., elastic deformations) using either nonpenetrating or penetrating liquids under hydrostatic pressure[53,56,88–92] with relatively small energies absorbed (∼10–60 J/g).[93–96] In contrast, irreversible, plastic deformations in MOFs, which can induce large volume collapse, have the potential to absorb much more mechanical energy during structural transition under high stresses, which has been investigated recently under both static and dynamic (i.e., shock) loading conditions thanks to the development of new experimental methods. The remainder of this review will focus on the consequences of irreversible changes in the structures of MOFs.

3.2.1 Nanocompression

Nanocompression is a powerful technique to measure the mechanical property of nanomaterials.[97] Specifically for MOFs, this technique allows measurement of mechanical parameters and energy absorption of individual nanocrystals at loadings of GPa without complications from interparticle interactions and macroscopic defects. It is usually operated inside a scanning electron microscope (SEM) or transmission electron microscope (TEM), where a μm-sized flat punch applies uniaxial compression on the sample (even a single nanocrystal) to provide load–displacement data while simultaneously recording the morphological evolution of the sample by in situ microvideography inside an electron microscope (Fig. 5).

The Suslick group observed the plastic deformation and mechanical behavior of individual ZIF-8 microcrystals using an in situ TEM nanocompression device.[98] In the nanocompression test, a diamond punch continuously compresses the ZIF-8 crystal without obvious cracking or

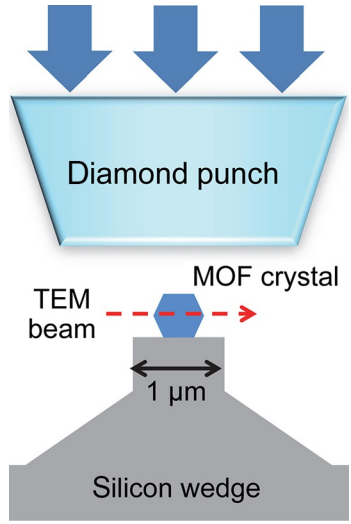

Fig. 5 Nanocompression for in situ uniaxial compression within a TEM. Loading force is measured by a piezo-actuator pressing the diamond punch against the sample crystal.

fracture, until the microcrystal was completely flattened at a maximum load of approximately 4400 μN, and the punch was then retracted from the pancaked crystal (Fig. 6). Huge deformation and volume reduction were observed during the compression process, which corresponds to the compression of internal void volume and amorphization. As a characteristic parameter of mechanical stability, Young's modulus was calculated at each stage of compression. The loading modulus (E_{load}) of 4.6 ± 0.2 GPa is close to the value previously reported from indentation experiments on large single crystals (2.9–3.2 GPa).[28] The unloading modulus (E_{unload}), however, is much larger (41 ± 4 GPa) as a consequence of the dense, amorphous structure generated from ZIF-8 at the maximum compression. This very large change in the modulus is an indication of the unique mechanical properties of MOFs that originate from their high porosity.

Interestingly, the mechanical properties of the ZIF-8 microcrystals are dramatically changed by the presence of guest solvate molecules within the pores, as demonstrated by compression tests on methanol-loaded ZIF-8 microcrystals. Compared to desolvated ones, the methanol solvated microcrystals are much more brittle and shatter completely at very low applied loads (~600 μN).

Nanocompression was also performed on nanocrystals of four UiO-type isostructural MOFs with varied linker length and pore sizes (specifically

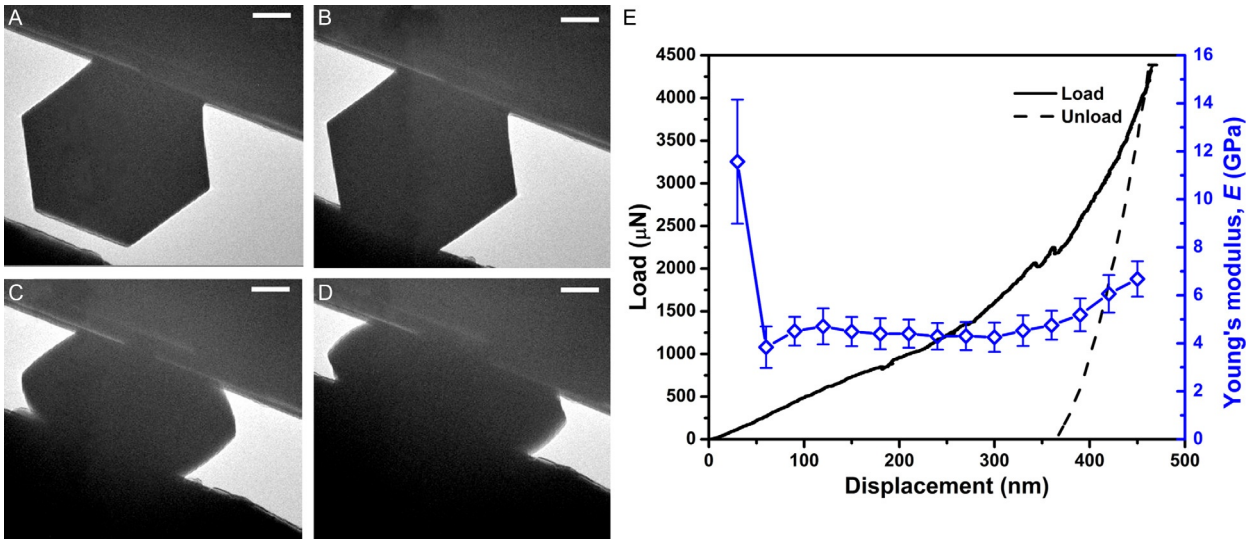

Fig. 6 (A–D) TEM images of a ZIF-8 microcrystal uniaxially compressed during the test at various displacements: (A) before contact, (B) 60 nm, (C) 270 nm, and (D) 390 nm. All scale bars are 200 nm. (E) Representative load–displacement curve of a nanocompression test on a 1.2 μm ZIF-8 microcrystal (left axis, *black line*) and calculated Young's modulus as a function of the displacement (right axis, *blue* or *gray line*). *Reprinted with permission from Su, Z.; Miao, Y.-R.; Mao, S.-M.; Zhang, G.-H.; Dillon, S.; Miller, J. T.; Suslick, K. S.* J. Am. Chem. Soc. ***2015***, 137, *1750–1753. Copyright 2015 American Chemical Society.*

MOF-801, UiO-66, UiO-67, and UiO-abdc) to evaluate the mechanical energy absorbed by MOFs during their plastic deformation (Figs. 7–9).[99] The loading Young's modulus E_{load} generally decreases as the linker length increase as predicted by calculation.[100] There is a notable exception with MOF-801, which is the most compressible in spite of having the shortest linker among the series: NMR analysis of a digested sample demonstrated that as-prepared MOF-801 contains a high concentration of defects from substitution of monocarboxylate ligands that were added as "modulators" as part of the synthesis of MOF-801. It is noteworthy that structural defects in UiO MOFs have been frequently reported[101–103] and would be expected to reduce the framework stability.[104,105] A recent study[106] on the kinetics of ball milling amorphization of Zr MOFs including UiO-66 also reported an inverse relationship between framework robustness and porosity, but again the presence of monocarboxylate modulators can complicate resistance to amorphization.

In contrast, the *unloading* modulus E_{unload}, which represents a mechanical property of the *densified* MOF structure, is not affected by defect density in the as-prepared MOF. In all the MOFs, the unloading modulus is linearly correlated with the applied maximum stress, indicating the structure

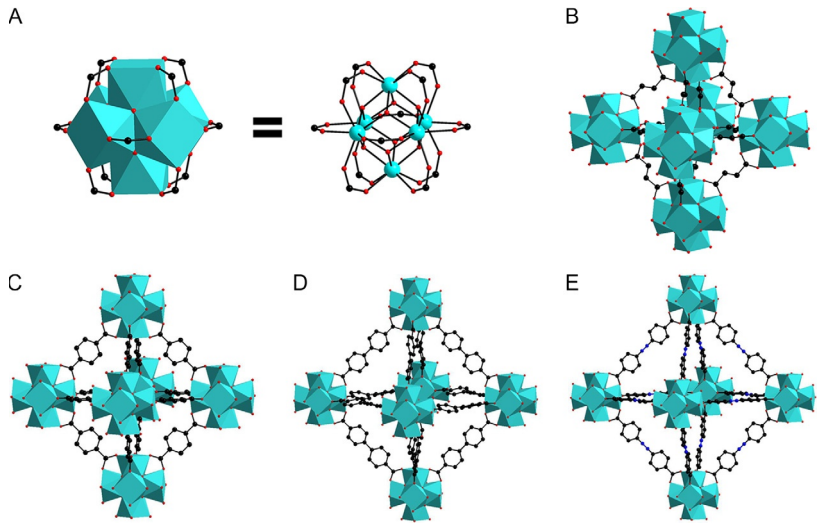

Fig. 7 Structures of (A) the $Zr_6O_4(OH)_4$ cluster in UiO-type MOFs, (B) MOF-801, (C) UiO-66, (D) UiO-67, and (E) UiO-abdc, with the corresponding dicarboxylic acid precursors below each structure. Zr: turquoise, C: *black*, O: *red*, N: *blue*; H omitted for clarity. *Reprinted with permission from Miao, Y. R.; Su, Z.; Suslick, K. S.* J. Am. Chem. Soc. ***2017***, 139, *4667–4670. Copyright 2017 American Chemical Society.*

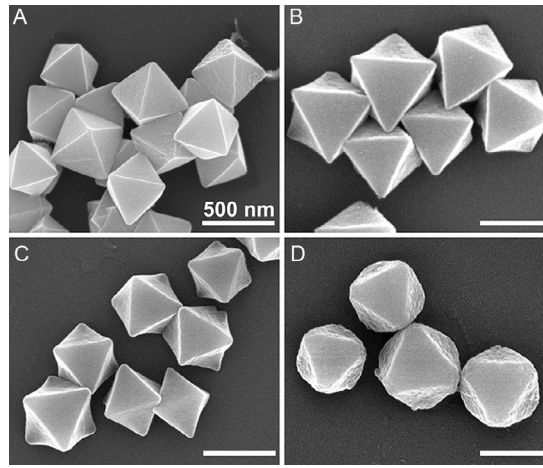

Fig. 8 SEM images of nanocrystals of (A) MOF-801, (B) UiO-66, (C) UiO-67, and (D) UiO-abdc; all scale bars indicate 500 nm. *Reprinted with permission from Miao, Y. R.; Su, Z.; Suslick, K. S.* J. Am. Chem. Soc. ***2017***, 139, *4667–4670. Copyright 2017 American Chemical Society.*

densification and amorphization can significantly increase the mechanical strength of these MOFs.

During each cycle, the absorbed mechanical energy can be calculated as $E = \int F dh$ by directly integrating the load–displacement curve (e.g., Fig. 6). In the low stress range (<2 GPa except MOF-801), the UiO MOFs absorb relatively small amounts of energy (<0.05 kJ/g), implying the deformation up to that point is predominantly elastic and reversible. The mechanical energy absorbed increases substantially as stress increases above 2 GPa, and at high applied pressures (>8 GPa), the energy absorbed, E_f, generally reaches up to 3–4 kJ/g for the UiO series MOFs under our experimental conditions (Fig. 9).[99] For comparison, the energy *released* in an explosion of TNT is ~4 kJ/g. Gram for gram, MOFs can absorb as much energy as a high explosive can release! Energy absorption during compression of bulk MOF solids may include contributions from normal strain, shear strain, powder packing, as well as pore volume collapse. Because only normal strain and volume collapse are measured in our single-crystal experiments, our results present a lower-bound estimate of the energy absorption capacity of MOFs.

For comparison, we may contrast the mechanical behavior of MOFs to ceramic materials. Similar nanocompression experiments were performed on ~500 nm octahedral nanocrystals of Cu_2O prepared as reported. While

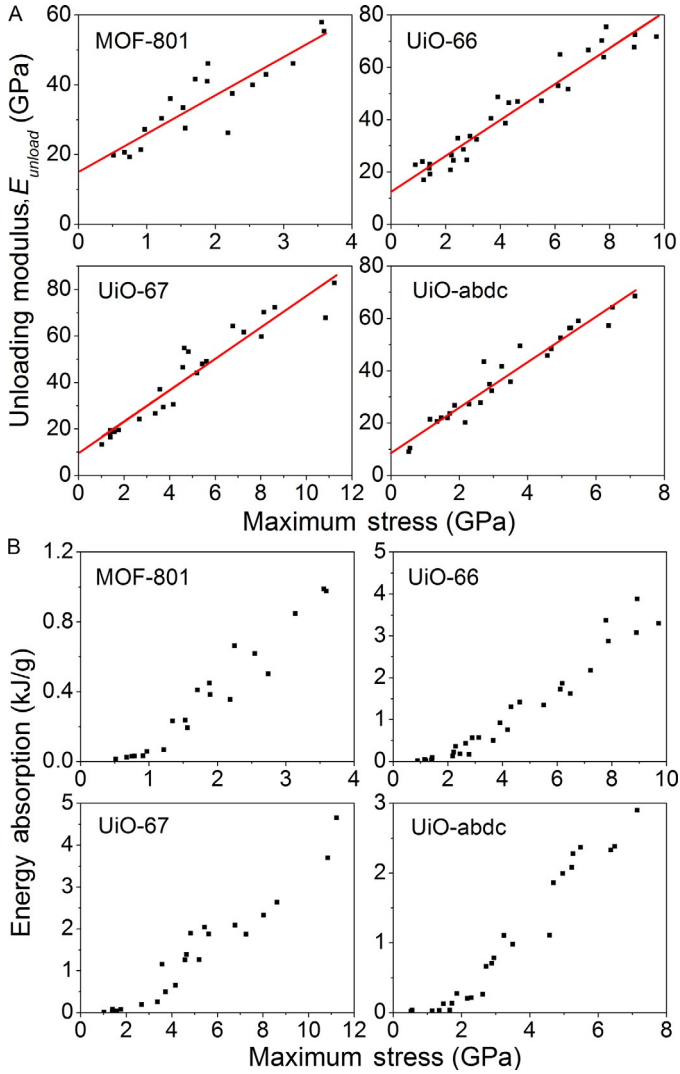

Fig. 9 (A) Unloading modulus (E_{unload}) and (B) the mechanical energy absorption of UiO MOFs as a function of stress. *Reprinted with permission from Miao, Y. R.; Su, Z.; Suslick, K. S.* J. Am. Chem. Soc. ***2017***, 139, *4667–4670. Copyright 2017 American Chemical Society.*

the deformation in the first compression is highly elastic, the energy-absorbing hysteresis becomes obvious in the second cycle as the maximum pressure rises. Further increasing the load in the third cycle leads to yielding beyond the elastic limit and discontinuity events, with the development of banding due to local stress in the nanoparticle as can be seen from the in situ

TEM images.[99] The energy absorption in the nanoparticle is only 59 J/g even when completely flattened, as compared to the kJ/g scale in MOF at similar strains. Likewise, compression experiments on CeO_2 nanoparticles show similar behavior and ductile deformation with very low energy absorption. These comparisons emphasize the unique mechanical behavior of MOFs.

3.2.2 Mechanochemical Reactions During Nanocompression

The internal free volume of porous materials diminishes upon exposure to mechanical compression,[107,108] with potential chemical consequences. When MOFs are subjected to strong compression, large negative ΔV and positive ΔS are expected due to the collapse of its internal free volume and the loss of crystallinity.[92,98,99,109] Thus, one may speculate[109–111] that MOFs might function as lightweight protective materials to absorb mechanical energy from shockwaves by their collapse and by endothermic bond breakage during their collapse.

In the EXAFS spectrum for the uncompressed UiO-66 (Fig. 10A), two major peaks were observed. The first corresponds to the nearest neighbors of the Zr(IV) ion, i.e., the Zr–O shell; overlapping features at 1.5 and 1.8 Å (phase uncorrected distances) correspond to the $Zr–O_{\mu3\text{-}O}$ (Zr to bridging O atom) and $Zr–O_{COO}$ (Zr to O atom of the carboxylate) bonds, respectively, which have different bond lengths ($Zr–O_{\mu3\text{-}O} < Zr–O_{COO}$). The second intense peak at 3.1 Å is ascribed to the next-nearest neighbors, i.e., the Zr⋯Zr shell. After compression, EXAFS spectra show changes in the coordination environment around Zr(IV) in UiO-66 (Fig. 10C). The peaks at 1.8 and 3.1 Å dramatically decrease with increasing compression, which indicates the loss of $Zr–O_{COO}$ bonds and Zr⋯Zr contacts. After compression at 1.9 GPa, the coordination number of $Zr–O_{COO}$ decreased from 4 to ~2, as determined by EXAFS. Under the same compression, the IR spectra (Fig. 10B) confirmed loss of $Zr–O_{COO}$ through the conversion of carboxylate groups from *syn–syn* bridging coordination mode to monodentate ligation, as shown schematically in Fig. 10C. In contrast, the peak intensity at 1.5 Å (from the $Zr–O_{\mu3\text{-}O}$ bonds) stays the same regardless of the extent of compression, which implies that the inner $Zr–O_{\mu3\text{-}O}$ bonds (i.e., the core of the Zr_6O_4 cluster) were not affected by compression. The breakage of the $Zr–O_{COO}$ bonds (i.e., breakage of Zr–O bonds between the bridging terephthalates to the $Zr_6O_4(OH)_4$ clusters) is a consequence of changes forced upon the extended structure of MOFs as pore collapse occurs. Importantly, such bond breakage is significantly endothermic and provides a mechanism

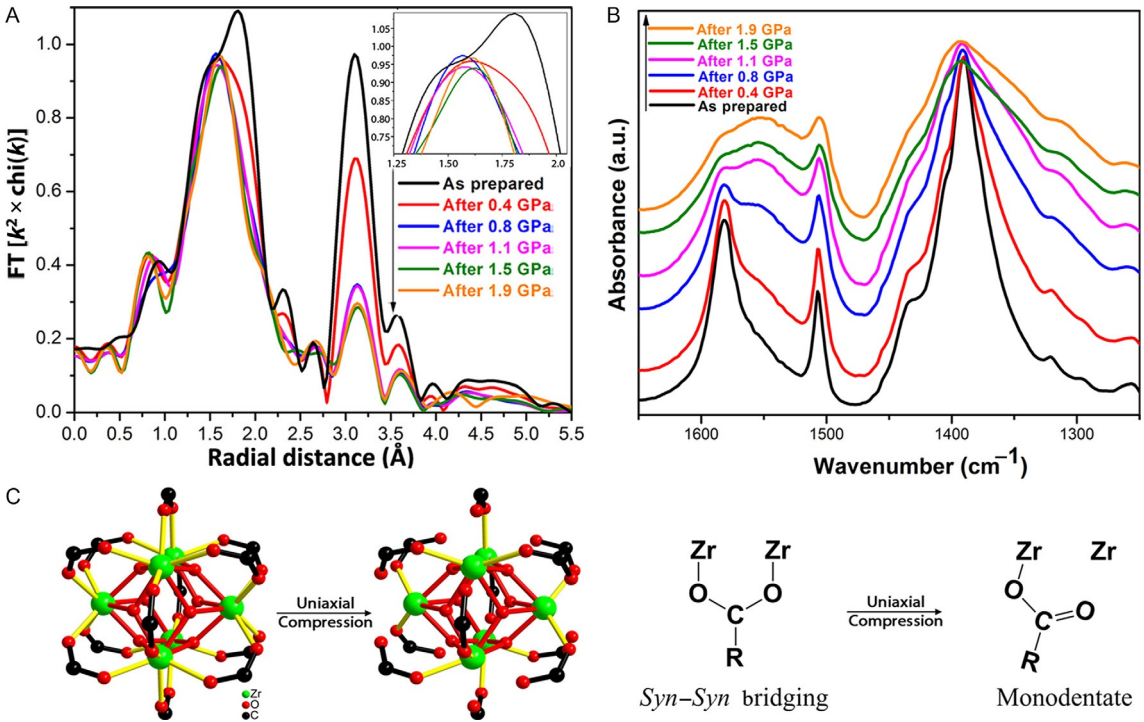

Fig. 10 Bond breakage in UiO-66 after bulk compression. (A) EXAFS spectra (magnitude of the k^2-weighted Fourier transform) of UiO-66 as prepared and after compression at various applied pressures. The peaks that diminish upon compression at 1.8 and 3.1 Å (phase uncorrected distances) are attributed to Zr–O_{coo} and Zr ⋯ Zr scatterers, respectively; the unchanged peak at 1.5 Å is from the Zr–$O_{\mu 3\text{-}O}$. (B) FTIR spectra of UiO-66 after compression and release; peak shift from 1580 to 1550 cm^{-1} corresponds to the coordination mode change of carboxylate groups. (C) Change in coordination mode of the bridging carboxylate within each Zr–O cluster in the UiO-66 upon compression (Unpublished work).

for the absorbance of large amounts of energy during irreversible plastic deformation resulting from compression.

The energy absorption capacity during mechanochemical reactions of UiO-66 depends on the intensity of the mechanical input. We performed static compression on bulk powder of UiO-66 to demonstrate quantitatively the effect of mechanical stress on the local bonding of MOFs. Assuming no other energy compensating effects are involved in the formation of the amorphorized structure, the energy absorbed from this endothermic bond breaking reaction is estimated to be 2.1 kJ/g. One may conclude that $Zr–O_{COO}$ bond breakage is the primary component of the large amount of energy absorbed during compressional collapse of UiO-66 that was discussed earlier.

3.2.3 Shock Wave Energy Dissipation

A shock wave is a mechanical compression or expansion that travels at supersonic speed.[112] It is characterized by a sudden jump of pressure, density, and internal energy at the wavefront, creating a dynamic environment with rapid compression loading and very high strain rate that inflicts damage in solids, including structures, equipment, and importantly, human bodies as well.[113] As such there is keen interest in developing new mechanisms for shock-protective materials.[114,115] Compared to dense solids, porous materials show distinct shock response in that they have a large free volume to compress when subjected to mechanical stress above the elastic limit. This volume collapse converts the mechanical work of shock wave into waste heat, thus can be potentially employed in shock attenuation applications.[116] So far, there are few reports on the direct experimental measurement of dynamic shock compression of MOFs, despite the large body of research devoted to static compression study.

In a recent study, Dlott, Suslick, and coworkers investigated the possibility of incorporating shock-absorbing chemical functionality in the form of nanoporous materials.[109] Many shock absorbing materials (such as sand or foam) function by compactification of void spaces[114,117]; by extending this mechanism down to the nm scale, we may be able to protect against shocks by using their energy to drive otherwise harmless endothermic chemical reactions: this would weaken the shock by absorbing its energy and attenuating its effects by stretching out the remaining energy in time. Based on what is known about detonations, where exothermic chemistries sustain a shock wave, in attenuation we would expect the initial bond-breaking endothermic steps to happen promptly behind the shock front,

while the chemically stored shock energy would be released more gradually, as heat, as broken bonds reform.[109,118,119] To this end, we have examined the effects of shock on an archetypal MOF material in the hope that shock compression might also break massive numbers of chemical bonds, and indeed that proves to be true.[109]

The first experiment of shock wave impact on MOFs was reported by Wei et al.[120] The Cu-BTC was impacted by a Cu flyer plate launched from table-top gas gun system, and dynamic pressure was generated in the MOF ranging from 0.3 to 7.5 GPa. While the empty framework of Cu-BTC was crushed at 0.5 GPa as determined from PXRD, it was found that the inclusion of ferrocene (Fc) into Cu-BTC framework significantly enhanced the shock resistance by a factor of six, highlighting the relationship between shock response and porosity in materials.

Banlusan and Strachan investigated the simulated shock wave response of MOF-5 using MD with a reactive force field.[110] The dynamical shock loading results in a two-wave structure during shock wave propagation in MOF, in which a pore-collapse wave follows an elastic precursor wave (Fig. 11). The pore-collapse wave is responsible for the weakening of the leading elastic wave and thus dissipates the shock wave energy. This is in contrast to the usual one-wave pattern in dense solid material where pore-collapse energy attenuation pathways are not possible.

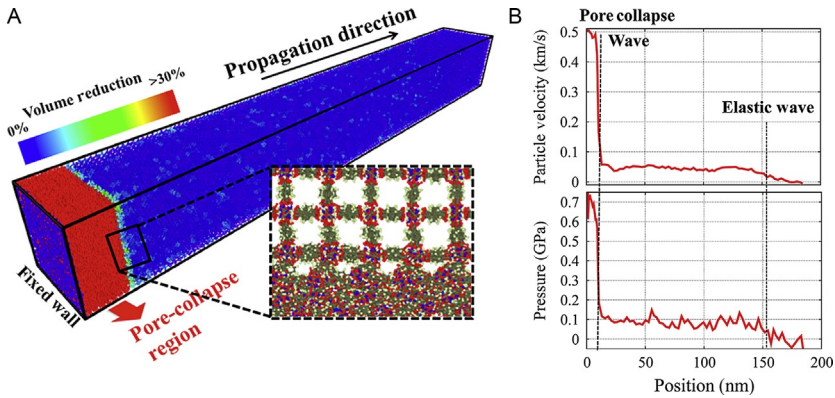

Fig. 11 Simulation results of shock wave propagation along [001] direction of MOF-5 with a piston speed of 0.5 km/s: (A) volume reduction and (inset) atomistic snapshot, showing the interface between irreversible pore collapse and the elastic region and (B) velocity and pressure profile near the wavefronts. *Reprinted with permission from Banlusan, K.; Strachan, A.* J. Phys. Chem. C ***2016***, 120, *12463–12471. Copyright 2016 American Chemical Society.*

The Dlott and Suslick groups examined the shock wave impact on the prototypical MOF ZIF-8[109] using a table-top laser-driven flyer plate system (Fig. 12).[121] In these experiments, the MOF sample is made as a uniform layer of ZIF-8 microcrystals on a gold-coated glass window. A pulsed laser causes ablation of a small piece of Al foil (the so-called "flyer plate") that impacts the MOF sample at a controlled velocity of 0–1.6 km/s, generating a shock wave that propagates through the ZIF-8 layer. Upon reaching the reflective gold coating, the shock wave is monitored by a photon Doppler velocimeter. As observed from the impacted samples, the ZIF-8 microcrystals undergo increasingly severe morphological change (including as fracture, fragmentation, and sintering) as the flyer impact strengthens (Fig. 13). XRD also reveals loss of crystallinity after shock compression. The postmortem FT-IR results confirm the 2-methylimidazolate (2-MeIm) group remains intact; the symmetry of the 2-MeIm, however, has been lowered and new peaks in the IR confirm asymmetric coordination (Fig. 14).

The in situ light emission measurements revealed more mechanistic details of the chemical effects of the shock compression. In the photoluminescence (PL) measurements, a 351 nm laser with a pulse duration of 200 ns was used to excite ZIF-8 with or without flyer plate impact. A resulting PL at 460 nm emission corresponds to the π–π^* transition of 2-MeIm ligand. For shock velocities <1.6 km/s, the signal is unaffected

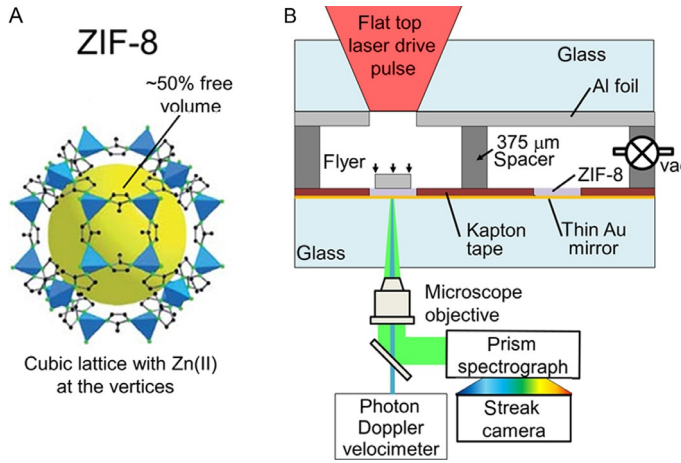

Fig. 12 (A) Crystal structure of ZIF-8 and (B) schematic of the table-top laser-driven flyer plate system. *Reprinted with permission from Su, Z.; Shaw, W. L.; Miao, Y. R.; You, S.; Dlott, D. D.; Suslick, K. S.* J. Am. Chem. Soc. ***2017***, 139, *4619–4622. Copyright 2017 American Chemical Society.*

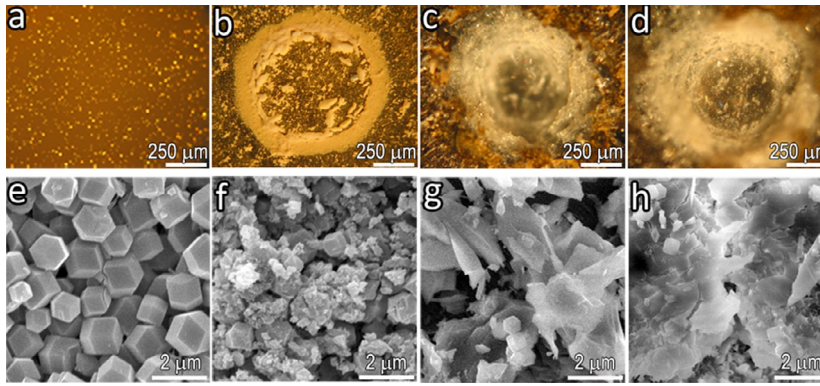

Fig. 13 The optical images (A–D) of ZIF-8 layer on glass and the SEM images (E–H) of ZIF-8 microcrystals after shock compression: (A and E) without shock, (B and F) 0.75 km/s (2.5 GPa), (C and G) 1.3 km/s (5 GPa), and (D and H) 1.6 km/s (8 GPa). *Reprinted with permission from Su, Z.; Shaw, W. L.; Miao, Y. R.; You, S.; Dlott, D. D.; Suslick, K. S.* J. Am. Chem. Soc. ***2017***, 139, *4619–4622. Copyright 2017 American Chemical Society.*

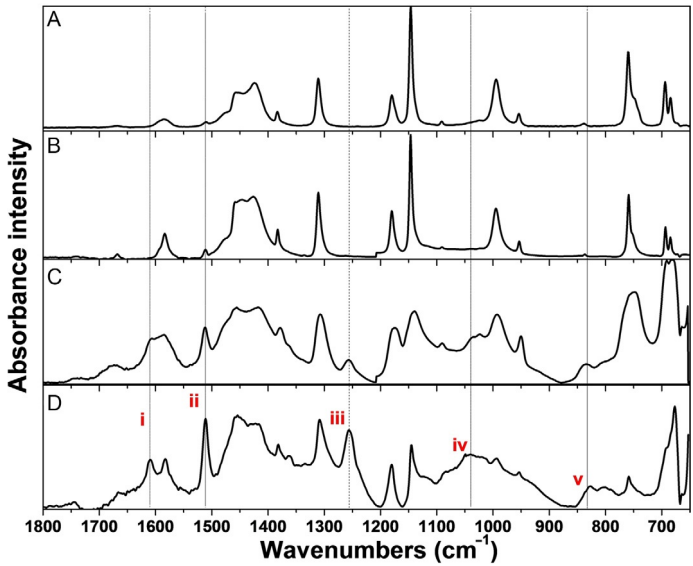

Fig. 14 IR spectra of ZIF-8 crystals (A) without impact, and after dynamic compression at (B) 0.75 km/s (2.5 GPa), (C) 1.3 km/s (5 GPa), and (D) 1.6 km/s (8 GPa). The *vertical lines* indicate the new peaks generated by shock compression. Peaks i, ii, iii, iv, and v are all associated with lowered symmetry of the 2-MeIm.[122] *Reprinted with permission from Su, Z.; Shaw, W. L.; Miao, Y. R.; You, S.; Dlott, D. D.; Suslick, K. S.* J. Am. Chem. Soc. ***2017***, 139, *4619–4622. Copyright 2017 American Chemical Society.*

by the shock, implying no significant structural change (consistent with Fig. 14). In contrast, at velocities >1.6 km/s (e.g., 1.9 km/s), the PL is suddenly quenched when the ZIF-8 is impacted, consistent with aggravated structural damage under high velocity shock impact. Simultaneously, shock-induced emission of ZIF-8 was clearly observed in separate experiments without an excitation laser. It is noteworthy that the emission did not appear during the shock, but rather long after the shock had passed, 50 ns after impact; the origin of the emission may be the highly exothermic recombination of energetic species generated by shock-induced bond breakage along with the structural collapse.

In summary, the shock compression of MOFs induced by km/s flyer plate impacts on ZIF-8 crystals can have substantial mechanochemical consequences.[109] The ZIF-8 crystals can maintain their crystalline structure with shocks below ≈2.5 GPa (flyer plate velocities of 0.75 km/s), but lose long-range crystalline order at ≈5 GPa (1.3 km/s) and undergo substantial morphological changes and fragmentation. Full structural collapse with loss of local symmetry occurs with shocks ≈8 GPa (1.6 km/s). Shocks from flyer plate impacts were much more devastating to the ZIF-8 crystal morphology than quasistatic DAC compression at comparable loading pressures even with a vastly shorter exposure time (nanoseconds vs minutes). Time resolved in situ PL and shock-induced emission indicate that the higher-velocity impacts that destroy the ZIF-8 structure also produce dramatic chemical changes and create high-energy chemical species. At least part of the excess chemical energy generated by shock-induced bond scission can be released about 50 ns later (i.e., long after the shock) in an intense emission burst. Thus high-velocity impacts on ZIF-8 appear to be able to dissipate the energy of shock waves in two distinct ways, by the collapse of the nanoporous network and by endothermic shock-induced bond scission.

4. CONCLUSIONS

Many mechanical processes inherently involve chemistry, and mechanochemistry has a long, rich history. With the expanding library of MOF structures and the development of characterization techniques, the study into the mechanochemistry of MOFs has led to an emerging field that correlates structure, property, and applications of these increasingly important materials. Originating from the unique structure, a range of exotic mechanochemical behaviors of MOFs has been discovered, suggesting real potential in applications such as mechanical energy storage and mechanical control

of guest release or uptake. Mechanical stimulus, as a special form of energy input and as a tunable synthetic tool, also has the ability to trigger unusual chemistry and holds great promise for solvent-free synthesis and post-synthetic modification of MOFs.

In this review, we have explored the subtle relationship between the mechanical properties and structures of MOF solids and newly discovered mechanochemical reactions in MOFs, including first demonstration of compression-induced bond breakage in MOFs, as shown through EXAFS and confirmed by IR spectra. Endothermic bond breakage is a consequence of changes forced upon the extended structure of MOFs as pore collapse occurs under pressure. The nature of bond breakage has been quantitatively investigated as a function of the compressional pressure using in situ nanocompression and electronic microscopy, which has provided structural information about the transition during compression. In these nanocompression experiments, substantial energy was irreversibly absorbed in the solids during collapse, comparable in magnitude to the energy *released* by typical explosives on a gram for gram basis.

ACKNOWLEDGMENTS

We acknowledge funding through the US Navy (MURI N000141210828) and the use of the Frederick Seitz Materials Research Laboratory Central Facilities, UIUC.

REFERENCES

1. Furukawa, H.; Cordova, K. E.; O'Keeffe, M.; Yaghi, O. M. *Science* **2013**, *341, 1230444.*
2. Zhou, H.-C.; Kitagawa, S. *Chem. Soc. Rev.* **2014**, *43*, 5415–5418.
3. Lee, J.; Farha, O. K.; Roberts, J.; Scheidt, K. A.; Nguyen, S. T.; Hupp, J. T. *Chem. Soc. Rev.* **2009**, *38*, 1450–1459.
4. Liu, J. W.; Chen, L. F.; Cui, H.; Zhang, J. Y.; Zhang, L.; Su, C. Y. *Chem. Soc. Rev.* **2014**, *43*, 6011–6061.
5. Murray, L. J.; Dinca, M.; Long, J. R. *Chem. Soc. Rev.* **2009**, *38*, 1294–1314.
6. Schneemann, A.; Bon, V.; Schwedler, I.; Senkovska, I.; Kaskel, S.; Fischer, R. A. *Chem. Soc. Rev.* **2014**, *43*, 6062–6096.
7. O'Keeffe, M.; Yaghi, O. M. *Chem. Rev.* **2012**, *112*, 675–702.
8. Zhou, H. C.; Long, J. R.; Yaghi, O. M. *Chem. Rev.* **2012**, *112*, 673–674.
9. Horike, S.; Umeyama, D.; Kitagawa, S. *Acc. Chem. Res.* **2013**, *46*, 2376–2384.
10. Furukawa, S.; Reboul, J.; Diring, S.; Sumida, K.; Kitagawa, S. *Chem. Soc. Rev.* **2014**, *43*, 5700–5734.
11. Cui, Y. J.; Li, B.; He, H. J.; Zhou, W.; Chen, B. L.; Qian, G. D. *Acc. Chem. Res.* **2016**, *49*, 483–493.
12. Farrusseng, D. Ed. *Metal-Organic Frameworks: Applications From Catalysis to Gas Storage*; Wiley-V C H Verlag Gmbh: Weinheim, 2011.
13. Li, J. R.; Kuppler, R. J.; Zhou, H. C. *Chem. Soc. Rev.* **2009**, *38*, 1477–1504.
14. Ma, S.; Zhou, H. C. *Chem. Commun. (Camb.)* **2010**, *46*, 44–53.

15. Li, J. R.; Sculley, J.; Zhou, H. C. *Chem. Rev.* **2012**, *112*, 869–932.
16. Suslick, K. S.; Bhyrappa, P.; Chou, J. H.; Kosal, M. E.; Nakagaki, S.; Smithenry, D. W.; Wilson, S. R. *Acc. Chem. Res.* **2005**, *38*, 283–291.
17. Kosal, M. E.; Chou, J. H.; Wilson, S. R.; Suslick, K. S. *Nat. Mater.* **2002**, *1*, 118–121.
18. Smithenry, D. W.; Wilson, S. R.; Suslick, K. S. *Inorg. Chem.* **2003**, *42*, 7719–7721.
19. Ma, L.; Abney, C.; Lin, W. *Chem. Soc. Rev.* **2009**, *38*, 1248–1256.
20. Farha, O. K.; Hupp, J. T. *Acc. Chem. Res.* **2010**, *43*, 1166–1175.
21. Kreno, L. E.; Leong, K.; Farha, O. K.; Allendorf, M.; Van Duyne, R. P.; Hupp, J. T. *Chem. Rev.* **2012**, *112*, 1105–1125.
22. Horcajada, P.; Gref, R.; Baati, T.; Allan, P. K.; Maurin, G.; Couvreur, P.; Ferey, G.; Morris, R. E.; Serre, C. *Chem. Rev.* **2012**, *112*, 1232–1268.
23. Della Rocca, J.; Liu, D.; Lin, W. *Acc. Chem. Res.* **2011**, *44*, 957–968.
24. Czaja, A. U.; Trukhan, N.; Muller, U. *Chem. Soc. Rev.* **2009**, *38*, 1284–1293.
25. Nandasiri, M. I.; Jambovane, S. R.; McGrail, B. P.; Schaef, H. T.; Nune, S. K. *Coord. Chem. Rev.* **2016**, *311*, 38–52.
26. Howarth, A. J.; Liu, Y.; Li, P.; Li, Z.; Wang, T. C.; Hupp, J. T.; Farha, O. K. *Nat. Rev. Mater.* **2016**, *1, 15018*.
27. Chapman, K. W.; Halder, G. J.; Chupas, P. J. *J. Am. Chem. Soc.* **2009**, *131*, 17546–17547.
28. Tan, J. C.; Bennett, T. D.; Cheetham, A. K. *Proc. Natl. Acad. Sci. U.S.A.* **2010**, *107*, 9938–9943.
29. Li, W.; Henke, S.; Cheetham, A. K. *APL Mater.* **2014**, *2, 123902*.
30. Coudert, F.-X. *Chem. Mater.* **2015**, *27*, 1905–1916.
31. Beyer, M. K.; Clausen-Schaumann, H. *Chem. Rev.* **2005**, *105*, 2921–2948.
32. Ribas-Arino, J.; Marx, D. *Chem. Rev.* **2012**, *112*, 5412–5487.
33. Boldyreva, E. *Chem. Soc. Rev.* **2013**, *42*, 7719–7738.
34. Takacs, L. *Chem. Soc. Rev.* **2013**, *42*, 7649–7659.
35. Liang, J.; Fernandez, J. M. *ACS Nano* **2009**, *3*, 1628–1645.
36. Friscic, T.; James, S. L.; Boldyreva, E. V.; Bolm, C.; Jones, W.; Mack, J.; Steed, J. W.; Suslick, K. S. *Chem. Commun.* **2015**, *51*, 6248–6256.
37. Friscic, T. *Chem. Soc. Rev.* **2012**, *41*, 3493–3510.
38. James, S. L.; Adams, C. J.; Bolm, C.; Braga, D.; Collier, P.; Friscic, T.; Grepioni, F.; Harris, K. D. M.; Hyett, G.; Jones, W.; Krebs, A.; Mack, J.; Maini, L.; Orpen, A. G.; Parkin, I. P.; Shearouse, W. C.; Steed, J. W.; Waddell, D. C. *Chem. Soc. Rev.* **2012**, *41*, 413–447.
39. May, P. A.; Moore, J. S. *Chem. Soc. Rev.* **2013**, *42*, 7497–7506.
40. Suslick, K. S. *Faraday Discuss.* **2014**, *170*, 411–422.
41. Wiggins, K. M.; Brantley, J. N.; Bielawski, C. W. *Chem. Soc. Rev.* **2013**, *42*, 7130–7147.
42. Wang, G.-W. *Chem. Soc. Rev.* **2013**, *42*, 7668–7700.
43. Ralphs, K.; Hardacre, C.; James, S. L. *Chem. Soc. Rev.* **2013**, *42*, 7701–7718.
44. Kole, G. K.; Vittal, J. J. *Chem. Soc. Rev.* **2013**, *42*, 1755–1775.
45. Groote, R.; Jakobs, R. T. M.; Sijbesma, R. P. *Polym. Chem.* **2013**, *4*, 4846–4859.
46. Braga, D.; Maini, L.; Grepioni, F. *Chem. Soc. Rev.* **2013**, *42*, 7638–7648.
47. Noji, H.; Okuno, D.; Ikeda, T. *Chem. Sci.* **2011**, *2*, 2086–2093.
48. Soboyejo, W. *Mechanical Properties of Engineered Materials*; CRC Press, 2002.
49. Wachtman, J. B.; Cannon, W. R.; Matthewson, M. J. *Mechanical Properties of Ceramics*; John Wiley & Sons, Inc, 2009; pp 1–25.
50. Merrill, L.; Bassett, W. A. *Rev. Sci. Instrum.* **1974**, *45*, 290–294.
51. Moggach, S. A.; Allan, D. R.; Parsons, S.; Warren, J. E. *J. Appl. Cryst.* **2008**, *41*, 249–251.

52. Tyagi, A. K.; Banerjee, S., Eds. *Materials Under Extreme Conditions: Recent Trends and Future Prospects*; Elsevier: Oxford, 2017.
53. Hobday, C. L.; Marshall, R. J.; Murphie, C. F.; Sotelo, J.; Richards, T.; Allan, D. R.; Duren, T.; Coudert, F. X.; Forgan, R. S.; Morrison, C. A.; Moggach, S. A.; Bennett, T. D. *Angew. Chem. Int. Ed.* **2016**, *55*, 2401–2405.
54. Cai, W.; Gładysiak, A.; Anioła, M.; Smith, V. J.; Barbour, L. J.; Katrusiak, A. *J. Am. Chem. Soc.* **2015**, *137*, 9296–9301.
55. Lanza, A.; Germann, L. S.; Fisch, M.; Casati, N.; Macchi, P. *J. Am. Chem. Soc.* **2015**, *137*, 13072–13078.
56. Im, J.; Yim, N.; Kim, J.; Vogt, T.; Lee, Y. *J. Am. Chem. Soc.* **2016**, *138*, 11477–11480.
57. Spencer, E. C.; Angel, R. J.; Ross, N. L.; Hanson, B. E.; Howard, J. A. K. *J. Am. Chem. Soc.* **2009**, *131*, 4022–4026.
58. Spencer, E. C.; Kiran, M. S.; Li, W.; Ramamurty, U.; Ross, N. L.; Cheetham, A. K. *Angew. Chem. Int. Ed.* **2014**, *53*, 5583–5586.
59. McKellar, S. C.; Graham, A. J.; Allan, D. R.; Mohideen, M. I. H.; Morris, R. E.; Moggach, S. A. *Nanoscale* **2014**, *6*, 4163–4173.
60. Bennett, T. D.; Cao, S.; Tan, J. C.; Keen, D. A.; Bithell, E. G.; Beldon, P. J.; Friscic, T.; Cheetham, A. K. *J. Am. Chem. Soc.* **2011**, *133*, 14546–14549.
61. Užarević, K.; Halasz, I.; Friščić, T. *J. Phys. Chem. Lett.* **2015**, *6*, 4129–4140.
62. Beldon, P. J.; Fábián, L.; Stein, R. S.; Thirumurugan, A.; Cheetham, A. K.; Friščić, T. *Angew. Chem. Int. Ed.* **2010**, *49*, 9640–9643.
63. Bennett, T. D.; Cheetham, A. K. *Acc. Chem. Res.* **2014**, *47*, 1555–1562.
64. Bennett, T. D.; Tan, J.-C.; Yue, Y.; Baxter, E.; Ducati, C.; Terrill, N. J.; Yeung, H. H. M.; Zhou, Z.; Chen, W.; Henke, S.; Cheetham, A. K.; Greaves, G. N. *Nat. Commun.* **2015**, *6*, 8079.
65. Katsenis, A. D.; Puškarić, A.; Štrukil, V.; Mottillo, C.; Julien, P. A.; Užarević, K.; Pham, M.-H.; Do, T.-O.; Kimber, S. A. J.; Lazić, P.; Magdysyuk, O.; Dinnebier, R. E.; Halasz, I.; Friščić, T. *Nat. Commun.* **2015**, *6*, 6662.
66. Halasz, I.; Kimber, S. A. J.; Beldon, P. J.; Belenguer, A. M.; Adams, F.; Honkimäki, V.; Nightingale, R. C.; Dinnebier, R. E.; Friščić, T. *Nat. Protoc.* **2013**, *8*, 1718–1729.
67. Friščić, T.; Halasz, I.; Beldon, P. J.; Belenguer, A. M.; Adams, F.; Kimber, S. A. J.; Honkimäki, V.; Dinnebier, R. E. *Nat. Chem.* **2013**, *5*, 66–73.
68. Julien, P. A.; Užarević, K.; Katsenis, A. D.; Kimber, S. A. J.; Wang, T.; Farha, O. K.; Zhang, Y.; Casaban, J.; Germann, L. S.; Etter, M.; Dinnebier, R. E.; James, S. L.; Halasz, I.; Friščić, T. *J. Am. Chem. Soc.* **2016**, *138*, 2929–2932.
69. Tan, J.-C.; Civalleri, B.; Lin, C.-C.; Valenzano, L.; Galvelis, R.; Chen, P.-F.; Bennett, T. D.; Mellot-Draznieks, C.; Zicovich-Wilson, C. M.; Cheetham, A. K. *Phys. Rev. Lett.* **2012**, *108, 095502.*
70. Ortiz, A. U.; Boutin, A.; Fuchs, A. H.; Coudert, F.-X. *J. Phys. Chem. Lett.* **2013**, *4*, 1861–1865.
71. Cao, S.; Bennett, T. D.; Keen, D. A.; Goodwin, A. L.; Cheetham, A. K. *Chem. Commun.* **2012**, *48*, 7805–7807.
72. Baxter, E. F.; Bennett, T. D.; Cairns, A. B.; Brownbill, N. J.; Goodwin, A. L.; Keen, D. A.; Chater, P. A.; Blanc, F.; Cheetham, A. K. *Dalton Trans.* **2016**, *45*, 4258–4268.
73. Bennett, T. D.; Simoncic, P.; Moggach, S. A.; Gozzo, F.; Macchi, P.; Keen, D. A.; Tan, J.-C.; Cheetham, A. K. *Chem. Commun.* **2011**, *47*, 7983–7985.
74. Hu, Y. H.; Zhang, L. *Phys. Rev. B* **2010**, *81, 174103.*
75. Banlusan, K.; Antillon, E.; Strachan, A. *J. Phys. Chem. C* **2015**, *119*, 25845–25852.
76. Bell, R.; et al. *Atlas of Zeolite Framework Types*; International Zeolite Association, 2017. http://www.iza-structure.org/ZFT_low_res.pdf.

77. Purewal, J. J.; Liu, D.; Yang, J.; Sudik, A.; Siegel, D. J.; Maurer, S.; Müller, U. *Int. J. Hydrogen Energy* **2012**, *37*, 2723–2727.
78. Kaye, S. S.; Dailly, A.; Yaghi, O. M.; Long, J. R. *J. Am. Chem. Soc.* **2007**, *129*, 14176–14177.
79. Ming, Y.; Purewal, J.; Yang, J.; Xu, C.; Soltis, R.; Warner, J.; Veenstra, M.; Gaab, M.; Müller, U.; Siegel, D. J. *Langmuir* **2015**, *31*, 4988–4995.
80. Peterson, G. W.; DeCoste, J. B.; Glover, T. G.; Huang, Y.; Jasuja, H.; Walton, K. S. *Microporous Mesoporous Mater.* **2013**, *179*, 48–53.
81. Peterson, G. W.; DeCoste, J. B.; Fatollahi-Fard, F.; Britt, D. K. *Ind. Eng. Chem. Res.* **2014**, *53*, 701–707.
82. Zheng, B.; Wang, L. L.; Hui, J. C.; Du, L.; Du, H.; Zhu, M. *Dalton Trans.* **2016**, *45*, 4346–4351.
83. Sava, D. F.; Rodriguez, M. A.; Chapman, K. W.; Chupas, P. J.; Greathouse, J. A.; Crozier, P. S.; Nenoff, T. M. *J. Am. Chem. Soc.* **2011**, *133*, 12398–12401.
84. Chapman, K. W.; Sava, D. F.; Halder, G. J.; Chupas, P. J.; Nenoff, T. M. *J. Am. Chem. Soc.* **2011**, *133*, 18583–18585.
85. Bennett, T. D.; Saines, P. J.; Keen, D. A.; Tan, J.-C.; Cheetham, A. K. *Chem. A Eur. J.* **2013**, *19*, 7049–7055.
86. Orellana-Tavra, C.; Baxter, E. F.; Tian, T.; Bennett, T. D.; Slater, N. K. H.; Cheetham, A. K.; Fairen-Jimenez, D. *Chem. Commun.* **2015**, *51*, 13878–13881.
87. Orellana-Tavra, C.; Marshall, R. J.; Baxter, E. F.; Lazaro, I. A.; Tao, A.; Cheetham, A. K.; Forgan, R. S.; Fairen-Jimenez, D. *J. Mater. Chem. B* **2016**, *4*, 7697–7707.
88. Chapman, K. W.; Halder, G. J.; Chupas, P. J. *J. Am. Chem. Soc.* **2008**, *130*, 10524–10526.
89. Graham, A. J.; Allan, D. R.; Muszkiewicz, A.; Morrison, C. A.; Moggach, S. A. *Angew. Chem. Int. Ed.* **2011**, *50*, 11138–11141.
90. Graham, A. J.; Banu, A.-M.; Düren, T.; Greenaway, A.; McKellar, S. C.; Mowat, J. P. S.; Ward, K.; Wright, P. A.; Moggach, S. A. *J. Am. Chem. Soc.* **2014**, *136*, 8606–8613.
91. McKellar, S. C.; Sotelo, J.; Mowat, J. P. S.; Wright, P. A.; Moggach, S. A. *CrstEngComm* **2016**, *18*, 1273–1276.
92. Moggach, S. A.; Bennett, T. D.; Cheetham, A. K. *Angew. Chem. Int. Ed.* **2009**, *48*, 7087–7089.
93. Ortiz, G.; Nouali, H.; Marichal, C.; Chaplais, G.; Patarin, J. *Phys. Chem. Chem. Phys.* **2013**, *15*, 4888–4891.
94. Ortiz, G.; Nouali, H.; Marichal, C.; Chaplais, G.; Patarin, J. *J. Phys. Chem. C* **2014**, *118*, 21316–21322.
95. Rodriguez, J.; Beurroies, I.; Loiseau, T.; Denoyel, R.; Llewellyn, P. L. *Angew. Chem. Int. Ed.* **2015**, *54*, 4626–4630.
96. Yot, P. G.; Vanduyfhuys, L.; Alvarez, E.; Rodriguez, J.; Itie, J.-P.; Fabry, P.; Guillou, N.; Devic, T.; Beurroies, I.; Llewellyn, P. L.; Van Speybroeck, V.; Serre, C.; Maurin, G. *Chem. Sci.* **2016**, *7*, 446–450.
97. Kiener, D.; Hosemann, P.; Maloy, S. A.; Minor, A. M. *Nat. Mater.* **2011**, *10*, 608–613.
98. Su, Z.; Miao, Y.-R.; Mao, S.-M.; Zhang, G.-H.; Dillon, S.; Miller, J. T.; Suslick, K. S. *J. Am. Chem. Soc.* **2015**, *137*, 1750–1753.
99. Miao, Y. R.; Su, Z.; Suslick, K. S. *J. Am. Chem. Soc.* **2017**, *139*, 4667–4670.
100. Yang, L.-M.; Ganz, E.; Svelle, S.; Tilset, M. *J. Mater. Chem. C* **2014**, *2*, 7111–7125.
101. Wu, H.; Chua, Y. S.; Krungleviciute, V.; Tyagi, M.; Chen, P.; Yildirim, T.; Zhou, W. *J. Am. Chem. Soc.* **2013**, *135*, 10525–10532.

102. Cliffe, M. J.; Wan, W.; Zou, X.; Chater, P. A.; Kleppe, A. K.; Tucker, M. G.; Wilhelm, H.; Funnell, N. P.; Coudert, F.-X.; Goodwin, A. L. *Nat. Commun.* **2014**, *5*, 4176.
103. Vermoortele, F.; Bueken, B.; Le Bars, G.; Van de Voorde, B.; Vandichel, M.; Houthoofd, K.; Vimont, A.; Daturi, M.; Waroquier, M.; Van Speybroeck, V.; Kirschhock, C.; De Vos, D. E. *J. Am. Chem. Soc.* **2013**, *135*, 11465–11468.
104. Thornton, A. W.; Babarao, R.; Jain, A.; Trousselet, F.; Coudert, F. X. *Dalton Trans.* **2016**, *45*, 4352–4359.
105. Rogge, S. M. J.; Wieme, J.; Vanduyfhuys, L.; Vandenbrande, S.; Maurin, G.; Verstraelen, T.; Waroquier, M.; Van Speybroeck, V. *Chem. Mater.* **2016**, *28*, 5721–5732.
106. Van de Voorde, B.; Stassen, I.; Bueken, B.; Vermoortele, F.; De Vos, D.; Ameloot, R.; Tan, J.-C.; Bennett, T. D. *J. Mater. Chem. A* **2015**, *3*, 1737–1742.
107. Green, R. *Int. J. Mech. Sci.* **1972**, *14*, 215–224.
108. Vafai, K. *Handbook of Porous Media*, 3rd ed.; Taylor & Francis Group: Boca Raton, FL, 2015.
109. Su, Z.; Shaw, W. L.; Miao, Y. R.; You, S.; Dlott, D. D.; Suslick, K. S. *J. Am. Chem. Soc.* **2017**, *139*, 4619–4622.
110. Banlusan, K.; Strachan, A. *J. Phys. Chem. C* **2016**, *120*, 12463–12471.
111. Yot, P. G.; Boudene, Z.; Macia, J.; Granier, D.; Vanduyfhuys, L.; Verstraelen, T.; Van Speybroeck, V.; Devic, T.; Serre, C.; Ferey, G.; Stock, N.; Maurin, G. *Chem. Commun.* **2014**, *50*, 9462–9464.
112. Forbes, J. W. *Shock Wave Compression of Condensed Matter: A Primer*; Springer Science & Business Media, 2013.
113. Kanel, G. I.; Razorenov, S. V.; Fortov, V. E. *Shock-Wave Phenomena and the Properties of Condensed Matter*; Springer-Verlag: NY, 2010.
114. Kapahi, A.; Udaykumar, H. *Shock Waves* **2013**, *23*, 537–558.
115. Qiao, P.; Yang, M.; Bobaru, F. *J. Aerosp. Eng.* **2008**, *21*, 235–248.
116. Antillon, E.; Strachan, A. *J. Chem. Phys.* **2015**, *142, 084108.*
117. Davison, L.; Horie, Y.; Shahinpoor, M. *High-Pressure Shock Compression of Solids IV: Response of Highly Porous Solids to Shock Loading*; Springer Science & Business Media, 2012.
118. Cherukara, M. J.; Germann, T. C.; Kober, E. M.; Strachan, A. *J. Phys. Chem. C* **2014**, *118*, 26377–26386.
119. Wood, M. A.; Cherukara, M. J.; Kober, E. M.; Strachan, A. *J. Phys. Chem. C* **2015**, *119*, 22008–22015.
120. Wei, Q.; Xu, H. W.; Yu, X. H.; Shimada, T.; Rearick, M. S.; Hickmott, D. D.; Zhao, Y. S.; Luo, S. N. *J. Appl. Phys.* **2011**, *110, 056102.*
121. Curtis, A. D.; Banishev, A. A.; Shaw, W. L.; Dlott, D. D. *Rev. Sci. Instrum.* **2014**, *85, 043908.*
122. Majoube, M.; Millié, P.; Vergoten, G. *J. Mol. Struct.* **1995**, *344*, 21–36.